Fe_2O_3 Nanoparticles within Mesoporous MCM-48 Silica: In Situ Formation and Characterization

Michael Fröba,* Ralf Köhn, and Gaëlle Bouffaud

Institute of Inorganic and Applied Chemistry, University of Hamburg, Martin-Luther-King-Platz 6, D-20146 Hamburg, Germany

Olivier Richard and Gustaaf van Tendeloo

EMAT, University of Antwerp, Groenenborgerlaan 171, B-2020 Antwerp, Belgium

Received April 12, 1999. Revised Manuscript Received July 16, 1999

Iron(III) oxide nanoparticles were synthesized within mesoporous MCM-48 silica phases. By using multiple cycles of wet impregnation, drying, and calcination procedures, it was possible to form haematite nanoparticles almost exclusively within the pore system. Nitrogen sorption measurements still revealed mesoporosity for the host/guest compound accompanied by a reduction of the BET surface area and the pore radius, both being indications of a decoration/coating of the inner surface of the silica walls. X-ray absorption spectroscopic measurements could prove the existence of small, slightly disordered iron(III) oxide nanoparticles. HRTEM investigations could show that the mesoporous host structure was still intact after the treatment. SAED (selected area electron diffraction) data did not reveal superstructure reflections or any diffuse intensity out of the Bragg reflections, indicating that the noncrystalline Fe_2O_3 is randomly distributed within the pores.

Introduction

In 1992, researchers from Mobil Oil Company introduced a new concept in the synthesis of porous materials by using a self-assembled molecular array of surfactant molecules as structure-directing template. In the case of silicates and aluminosilicates, the removal of these templates led to mesoporous molecular sieves with adjustable pore sizes ranging from 2 to 10 nm.[1,2] The arrangement of the pores is very regular, and the pore size distribution is nearly as sharp as that of conventional zeolites. Owing to these special pore properties, the materials, denoted as M41S phases, are of great interest for size- and shape-selective applications, e.g., catalysis, molecular sieves, or as host structures for nanometer-sized guest compounds. The M41S family is classified into several members. Depending on the shape of their supramolecular templates and the respective resulting pore structures, different phases can be distinguished: MCM-41 (hexagonal), MCM-48 (cubic), MCM-50 (lamellar), and other species. In case of silica, we have focused our work especially on the cubic MCM-48 phase. The surface-defining MCM-48 is the gyroid or G-surface, forming a structure with the space group $Ia\bar{3}d$,[3,4] which is frequently observed in water−surfactant systems.[5,6] The structure contains a three-dimensional network with channels running along [111] and [100], which provides large surface areas and a high accessibility of sites within the porous network structure even if part of the pore entrances cannot be used due to blockage,[7] which is a great advantage in comparison with the one-dimensional channel system of MCM-41. In contrast to results obtained by commonly used techniques, i.e., XRD and ^{29}Si NMR spectroscopy, X-ray absorption spectroscopic measurements at the Si K-edge proved that the pore walls are not entirely amorphous, but show a medium-range order (0.5−1.2 nm), comparable to the one in three-layer silicates, i.e., magadiite.[8,9] Besides dipole-allowed electronic transitions, the Si−K XANES (X-ray absorption near-edge structure) region is mainly determined by multiple-scattering effects, which can be used as a fingerprint in order to identify the respective compound.[10,11] Due to its special pore structure this cubic silica phase is very interesting as a

* Corresponding author.E-mail: Froeba@xray.chemie.uni-hamburg.de.

(1) Kresge, C. T.; Leonowicz, M. E.; Roth, W. J.; Vartuli J. C.; Beck, J. S. *Nature* **1992**, *359*, 710.

(2) Beck, J. S.; Vartuli, J. C.; Roth, W. J.; Leonowicz, M. E.; Kresge, C. T.; Schmitt, K. D.; Chu, C. T.-W; Olson, D. H.; Sheppard, E. W.; McCullen, S. B.; Higgins J. B.; Schlenker, J. L. *J. Am. Chem. Soc.* **1992**, *114*, 10834.

(3) Schmidt, R.; Stöcker, M.; Akporiaye, D.; Torstad, E. H.; Olsen, A. *Microporous Mater.* **1995**, *5*, 1.

(4) Alfredsson, V.; Anderson, M. W.; Ohsuna, T.; Terasaki, O.; Jacob, M.; Bojrup, M. *Chem. Mater.* **1997**, *9*, 2066.

(5) Auvray, X.; Petipas, C.; Anthore, R.; Rico, I.; Lattes, A. J. *J. Phys. Chem.* **1989**, *93*, 7458.

(6) Funari, S. S.; Rapp, *G. J. Phys. Chem. B* **1997**, *101*, 732.

(7) Monnier, A.; Schüth, F.; Huo, Q.; Kumar, D.; Margolese, D.; Maxwell, R. S.; Stucky, G. D.; Krishnamurty, M.; Petroff, P.; Firouzi, A.; Janicke, M.; Chmelka, B. F. *Science* **1993**, *261*, 1299.

(8) Fröba, M.; Behrens, P.; Wong, J.; Engelhardt, G.; Haggenmüller, Ch.; van de Goor, G.; Rowen, M.; Tanaka, T.; Schwieger, W. *Mater. Res. Soc. Symp. Proc.* **1995**, *371*, 99.

(9) Fröba, M.; Pillep, B.; Engelhardt, G.; Haggenmüller, Ch.; Wong, J.; Rowen, M.; Tanaka, T.; Schwieger, W.; Behrens, P. *Chem. Mater.* **1999**, in preparation.

(10) Fröba, M.; Wong, J.; Behrens, P.; Sieger, P.; Rowen, M.; Tanaka, T.; Rek, Z.; Felsche, J. *Physica B* **1995**, *208* & *209*, 65.

(11) Fröba, M.; Wong, J.; Rowen, M.; Brown, G. E., Jr.; Tanaka, T.; Rek, Z. *Physica B* **1995**, *208* & *209*, 555.

10.1021/cm991048i CCC: $18.00
Published on Web 09/11/1999

matrix to immobilize catalytically active species,[12] e.g., Ti,[13,14] V,[15,16] Mn,[17] Al,[18−20] Fe,[21] Cu,[22,23] and Zr[24] onto or within the silica walls or as a host to accommodate certain guest compounds.[25] In comparison to MCM-41, the synthesis of MCM-48 is more difficult, which is the molecular reason, why most of the interest in mesoporous sieves has been concentrated almost exclusively on MCM-41 in the past, and very little information was available on MCM-48. Recently, research groups have started to optimize the synthesis of the cubic phase[26−31] and it was even possible to obtain MCM-48 single crystals.[32]

Previous attempts to introduce nanoparticles on the basis of iron(III) or Fe_2O_3 particles into M41S materials were limited to the hexagonal MCM-41 phase,[33,34] and in none of these cases direct solid proof was given that the nanoparticles have been incorporated into the pore structure.

Experimental Section

The MCM-48 silica was synthesized from a mixture of reactants with the following composition: 1.0 tetraethyl orthosilicate (TEOS):0.65 cetyltrimethylammonium bromide (CTAB): 0.5 KOH:62 H_2O. After stirring for 10−30 min to homogenize the synthesis mixture, the mixture was filled into a Teflon-lined steel autoclave and statically heated at 388 K for 48 h. The resultant white product was filtered and washed several times with deionized water. After drying it was calcined at 823 K in air for 6 h within a programmable furnace of the company GERO type F 40−500/1300C. The loading of iron oxides onto the inner surface of MCM-48 was carried out by the wet impregnation technique (stirring at room temperature for 10 min) with 1.6 M aqueous solution of iron(III) nitrate ($Fe(NO_3)_3 \cdot 9H_2O$). After each impregnation step (maximum of three), the resulting product was washed with deionized water and dried at room temperature under vacuum for several hours. Afterward the material was calcined at 673 K under N_2 atmosphere for 6 h which led to a transformation of the iron nitrate into an oxide indicated by the disappearance of the IR band of the NO_3^- ion at 1380 cm^{-1}. To make sure that just haematite (α-Fe_2O_3) was formed under these experimental conditions, pristine iron(III) nitrate was treated in the same way and the brown powder obtained was identified as α-Fe_2O_3 by powder X-ray diffraction. Depending on the number of impregnation/calcination cycles an Fe content between 10 and 40 wt % was achieved.

Powder X-ray diffraction (XRD) was performed on a Philips PW 1050/25 diffractometer using filtered Cu Kα radiation. Data were collected after each step of the synthesis, first to confirm that the mesoporous MCM-48 structure has not been destroyed and second to examine that no separate condensed iron oxide phase has additionally been formed.

The BET surface areas and the pore diameters were determined by N_2 adsorption−desorption isotherms, which were recorded with a Sorptomatic 1000 (Carlo-Alba Instruments). The samples were outgassed at 150 °C for 24 h. The surface areas were calculated applying the BET equation for the relative pressures between 0.05 and 0.2. The pore size distributions were calculated using the desorption branch of the N_2 adsorption/desorption isotherm and the Barrett−Joyner−Halenda (BJH) formula.[35]

X-ray absorption spectroscopic measurements were carried out at the storage ring DORIS III (HASYLAB@DESY, Hamburg, Germany) at the EXAFS II beam line which was equipped with a Si(111) double-crystal monochromator. All spectra were recorded at 20 K in a conventional step-scanning mode. Each spectrum was calibrated against the first inflection point of the Fe K-edge (7112 eV) of an Fe metal foil which was measured simultaneously. As a reference compound, freshly prepared haematite[36] was used. All samples were prepared as pressed polyethylene pellets in which the Fe content was adjusted to yield an absorption jump of about 0.4−0.7. For further data analyses, the program WinXAS[37] was used. Theoretical calculations of the phase shifts and back-scattering amplitudes were calculated using FEFF6.01.[38]

For electron microscopic measurements the powders were crushed in ethanol, and the ground material was dispersed on a holey carbon grid. The electron diffraction and HRTEM studies were carried out using a Philips CM20 operating at 200 kV with a very low illumination to avoid destruction of the material under the electron beam. The EDS analyses were performed using a Link QX 20 analytical system.

Results and Discussion

X-ray Diffraction. The XRD pattern of the parent MCM-48 silica (**A**) shows the typical *hkl* reflections (Figure 1) which can be indexed in the cubic space group $Ia\bar{3}d$. With every impregnation/calcination cycle (samples **B**−**D**) the intensity of the X-ray reflections decreases accompanied by a slight shift to larger values 2θ and smaller *d* spacings, respectively (Figure 1). We attribute this effect to the influence of the impregnation/calcination cycles, which probably increase the degree of connectivity within the silica walls. As a result, this leads to a small contraction of the overall host structure, an effect consistent with literature reports that the mesoporous structure contracts upon calcination or

(12) Zhang, W. Z.; Pinnavaia, T. J. *Catal. Lett.* **1996**, *38*, 261.
(13) Morey, M.; Davidson, A.; Stucky, G. *Microporous Mater.* **1996**, *6*, 99.
(14) Koyano, K. A.; Tatsumi, T. *Chem. Commun.* **1996**, 145.
(15) Morey, M.; Davidson, A.; Eckert, H.; Stucky, G. *Chem. Mater.* **1996**, *8*, 486.
(16) Van Der Voort, P.; Morey, M.; Stucky, GD.; Mathieu, M.; Vansant, E. F. *J. Phys. Chem. B* **1998**, *102*, 585.
(17) Zhao, D. Y.; Goldfarb, D. *J. Chem. Soc., Chem. Commun.* **1995**, 875.
(18) Kosslick, H.; Lischke, G.; Landmesser, H.; Parlitz, B.; Storek, W.; Fricke, R. *J. Catal.* **1998**, *176*, 102.
(19) Schmidt, R.; Junggreen, H.; Stocker, M. *Chem. Commun.* **1996**, 875.
(20) Romero, A. A.; Alba, M. D.; Klinowski, J. *J. Phys. Chem. B* **1998**, *102*, 123.
(21) Echchahed, B.; Moen, A.; Nicholson, D.; Bonneviot, M. *Chem. Mater.* **1997**, *9*, 1716.
(22) Hartmann, M.; Racouchot, S.; Bischof, C. *Chem. Commun.* **1997**, 2367.
(23) Reller, A., Ebbinghaus, S.; Köhn, R.; Fröba, M.; Sazama, U.; Fortunato, P. *Mater. Res. Soc. Symp. Proc.* **1999**, *547*, 75.
(24) Morey, M.; Stucky, G. D.; Schwarz, S.; M. Fröba, M. *J. Phys. Chem. B* **1999**, *103*, 2037.
(25) Moller, K.; Bein, T. *Chem. Mater.* **1998**, *10*, 2950.
(26) Romero, A. A.; Alba, M. D.; Zhou, W.; Klinowski, J. *J. Phys. Chem. B* **1997**, *101*, 5294.
(27) Behrens, P.; Glaue, A.; Haggenmüller, Ch.; Schechner, G. *Solid State Ionics* **1997**, *101−103*, 255.
(28) Gallis, K. W.; Landry, C. C. *Chem. Mater.* **1997**, *9*, 2035.
(29) Corma, A.; Kann, Q.; Rey, F. *Chem. Commun.* **1998**, 579.
(30) Chen, F.; Huang, L.; Li, Q. *Chem. Mater.* **1997**, *9*, 2685.
(31) Xu, J.; Luan, Z.; He, H.; Zhou, W.; Kevan, L. *Chem. Mater.* **1998**, *10*, 3690.
(32) Kim, J. M.; Kim, S. K.; Ryoo, R. *Chem. Commun.* **1998**, 259.
(33) Yuan, Z. Y.; Liu, S. Q.; Chen, T. H.; Wang, J. Z.; Li, H. X. *J. Chem. Soc., Chem. Commun.* **1995**, 973.
(34) Abe, T.; Tachibana, Y.; Uematsu, T.; Iwamoto, M. *J. Chem. Soc., Chem. Commun.* **1995**, 1617.
(35) Barrett, E. P.; Joyner, L. G.; Halenda, P. P. *J. Am. Chem. Soc.* **1951**, *73*, 373.
(36) Schwertmann, U.; Cornell, R. M. *Iron Oxides in the Laboratory − Preparation and Characterization*; VCH Verlagsgesellschaft: Weinheim, 1991.
(37) Ressler, T. *J. Synchrotron Rad.* **1998**, *5*, 118.
(38) Rehr, J. J.; Mustre de Leon, J.; Zabinsky, S. I.; Albers, R. C. *J. Am. Chem. Soc.* **1991**, *113*, 5135.

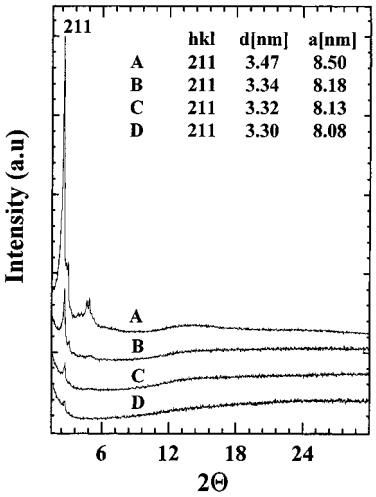

Figure 1. X-ray diffractograms of the parent MCM-48 silica material (**A**) and the respective host/guest compounds after the first (**B**), second (**C**), and third (**D**) impregnation/calcination cycle. The *d* spacing of the (211) reflection is listed together with the corresponding lattice constant a.

treatment in acidic solutions.[39] The strong reduction of the X-ray peak intensities is due to increasing destructive interferences by filling the pores with rising amounts of the iron oxide. After each treatment with the iron(III) nitrate solution, all *hkl* reflections are extinct, but reappear after the drying and in situ formation of the haematite in the course of calcination. In general, the introduction of scattering material into the pores leads to an increased phase cancellation between scattering from the wall and the pore regions and therefore to reduced scattering intensities for the Bragg reflections.[40−42] First theoretical models have shown that this phase relationship is very sensitive and that the degree of cancellation is mainly determined by the scattering contrast between the framework walls and the pores.[43] Besides the typical MCM-48 silica reflections, no additional peaks are observed, indicating that no crystalline iron oxide phase has been formed outside the pore structure. With an average pore diameter of 2.8 nm, iron oxide particles synthesized within the pores would be too small to give X-ray reflections. As the most sensitive step in the synthesis of the host/guest compound, the drying procedure has to be considered. Best results are obtained by running the drying process at room temperature and under vacuum. Every attempt to use elevated temperatures (above 150 °C) under ambient pressure leads to the premature formation of haematite outside the pores as proved by XRD.

Nitrogen Sorption. Figure 2 shows the amount of nitrogen physisorbed at 77 K versus the relative pressure for the parent MCM-48 silica material (**A**) as well as for the host/guest compounds received after the first to third impregnation/calcination cycle (**B**−**D**). All isotherms are of type IV, typical of mesoporous materials.[44] A well-defined step occurs between approximately $p/p_0 = 0.2-0.3$, associated with the filling of the mesopores due to capillary condensation. Depending on the number of impregnation/calcination cycles, the amount of physisorbed nitrogen decreases accompanied with a shift of the inflection point of the step to smaller values of p/p_0. Both effects can be attributed to the introduction of the iron oxide nanoparticles into the mesopores. The reduced amount of physisorbed nitrogen is caused by a smaller specific surface, while the occurrence of the step at lower relative pressure is indicative of smaller pore sizes. At this point one has to be aware that the introduction of the heavy iron oxide itself leads already to a reduction of the specific surface of the mesoporous silica matrix (molecular weight: Fe_2O_3, 159.69; SiO_2, 60.08). The determined BET surface, the content of Fe_2O_3 together with the intrinsic reduction of the specific surface due to the inserted Fe_2O_3, as well as the calculated mean pore radius are listed in Table 1. In contrast to MCM-41-type adsorbents,[45] no appropriate pore model exists for MCM-48 silica materials which allows the calculation of pore size distributions of the basis of the very powerful density functional theory (DFT). Taking this into account, we decided to apply the BJH formula to our mesoporous M41S phases, knowing that this well-established method underestimates the pore size[46,47] by ∼1.0 nm.[48] Nevertheless, it allows the determination of relative changes of pore size distributions. To learn more about the pristine or even modified MCM-48 silica pore structure in particular, further sorption studies using different adsorbates, temperatures and pore sizes will be published elsewhere.[49] Due to a better mobility of the iron nitrate within the pores at the beginning, the largest reduction of the specific surface as well as of the pore radius occurs with the first impregnation/calcination cycle. With the in situ formation of the iron oxide, the step of the isotherms at $p/p_0 = 0.2-0.3$ is slightly broadening, representing a less uniform remaining pore size, which is probably caused by a small inhomogeneous filling of the pores. Nevertheless, all samples still show mesoporosity, which is indicative of a coating of the inner surface of MCM-48 silica rather than a complete filling of the pores.

X-ray Absorption Spectroscopy. X-ray absorption spectroscopic measurements at the Fe K-edge were carried out in order to obtain structural information on the iron coordination within the iron oxide nanoparticles. Considering the energy position of the absorption edge, the nanocomposites **B**−**D** appear at the same position as haematite, indicating a valence shift charac-

(39) Janicke, M.; Kumar, D.; Stucky, G. D.; Chmelka, B. F. In *Zeolites and Related Microporous Materials: State of the Art*; Weitkamp, J., Karge, H. G., Pfeifer, H., Hölderich, W., Eds.; Elsevier: Amsterdam, 1994; p 243.
(40) Marler, B.; Oberhagemann, U.; Vortmann, S.; Gies, H. *Microporous Mater.* **1996**, *6*, 375.
(41) Glinka, C. J.; Nicol, J. M.; Stucky, G. D.; Ramli, E.; Margolese, D.; Huo, Q.; Higgins, J. B.; Leonowicz, M. E. *J. Porous Mater.* **1996**, *3*, 93.
(42) Lim, M. H.; Blanford, C. F.; Stein, A. *Chem. Mater.* **1998**, *10*, 467.
(43) Hammond, W.; Prouzet, E.; Mahanti, S. D.; Pinnavaia, T. J. *Microporous Mesoporous Mater.* **1999**, *27*, 19.
(44) Sing, K. S. W.; Everett, D. H.; Haul, R. A. W.; Moscou, L.; Pierotti, R. A.; Rouquérol, J.; Siemieniewska, T. *Pure Appl. Chem.* **1985**, *57*, 603.
(45) Neimark, A. V.; Ravikovitch, P. I.; Grün, M.; Schüth, F.; Unger, K. K. *J. Colloid Interface Sci.* **1998**, *207*, 159.
(46) Lastoskie, C.; Gubbins, K. E.; Quirke, N. J. *J. Phys. Chem.* **1993**, *97*, 4786.
(47) Ravikovitch, P. I.; Domhnaill, S. C. O.; Neimark, A., Schüth, F.; Unger, K. K. *Langmuir* **1995**, *11*, 4765.
(48) Ciesla, U.; Schüth, F. *Microporous Mesoporous Mater.* **1999**, *27*, 131.
(49) Thommes, M.; Köhn, R.; Fröba, M. *Microporous Mesoporous Mater.* **1999**, submitted.

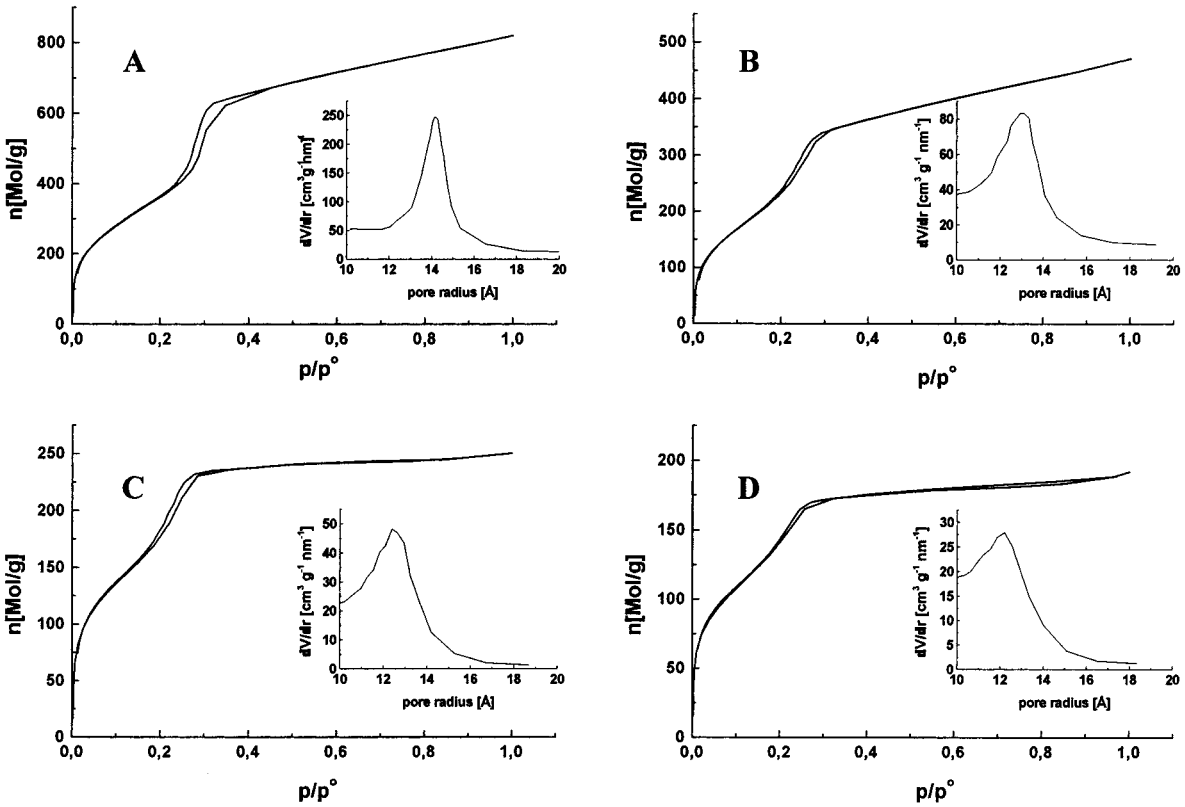

Figure 2. Nitrogen adsorption/desorption isotherms of the parent MCM-48 silica material (**A**) and the respective host/guest compounds after the first (**B**), second (**C**), and third (**D**) impregnation/calcination cycle. The insets show the pore radius distributions calculated from the analyses of the desorption branches of the isotherms.

Table 1. BET Surface Area, Fe_2O_3 Content, Reduction of the BET Surface Due to the Introduction of Iron Oxide and Mean Value of the Pore Radius Distribution of the Parent MCM-48 Silica Material (A) and the Respective Host/Guest Compounds after the First (B), Second (C), and Third (D) Impregnation/Calcination Cycle

sample	BET surface (m^2/g0	Fe_2O_3 content (weight %)/red. of BET surface (m^2/g)	mean pore radius (nm)
A	1376	−/−	1.42
B	866	19.6/270	1.31
C	681	32.1/442	1.26
D	509	42.5/585	1.22

teristic for iron(III); no iron(II) has been formed during the calcination procedure. In contrast to the crystalline haematite, the XANES (X-ray absorption near-edge structure) of the samples **B**−**D** are more smeared out and broadened (see Figure 3), an effect well-known from nanostructured materials with some kind of structural disorder.[50] All spectra show a small pre-edge peak caused by dipole-allowed electronic transitions. The relatively small intensity is an indication for octahedrally coordinated iron, which one would expect in case of haematite nanoparticles within the pores. An introduction of iron into the silica wall would mostly lead to a tetrahedral coordination and, as a result, to a much higher peak intensity.[21] In the following we focus our work on the analysis of the EXAFS (extended X-ray absorption fine structure) region. After conventional data analyses, i.e., energy calibration, background subtraction, and normalization of the edge-jump, the k^3-weighted data were Fourier transformed using a Bessel

(50) Fröba, M.; Muth, O. *Adv. Mater.* **1999**, *11*, 564.

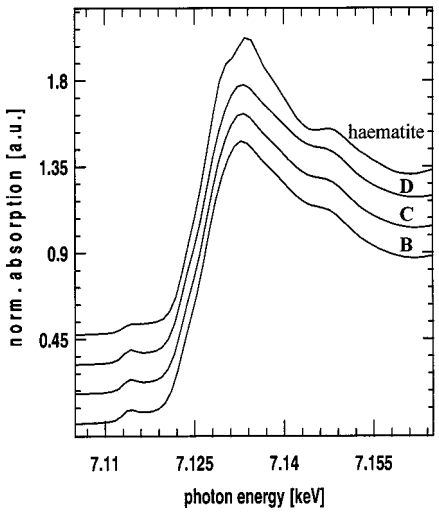

Figure 3. Normalized Fe K-XANES spectra of the host/guest compounds **B**−**D** and of a bulk sample of haematite.

window ranging from $k = 3$ to 15 Å^{-1}. Figures 4 and 5 show the EXAFS oscillations $\chi(k)*k^3$ and the corresponding Fourier transforms (FTs). In case of Figure 4, the amplitude of the EXAFS oscillation of the bulk haematite is multiplied by a factor of 0.3, which already indicates the strong intensity reduction in the backscattering amplitudes for the host/guest compounds due to the small particle sizes and the occurrence of some structural disorder. The loss of long-range order becomes even more visible in the FTs. While the radial distribution function of the haematite shows peaks at distances up to 7 Å, the FTs of the iron oxide nanoparticles indicate only the Fe−O and Fe−Fe coordination

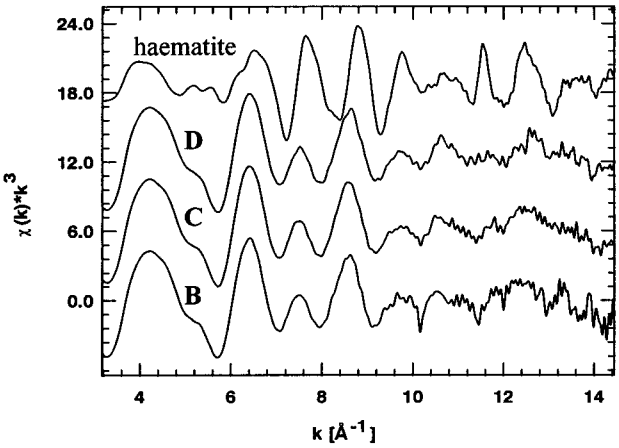

Figure 4. Fe K-edge EXAFS oscillations $\chi(k)*k^3$ of the host/guest compounds **B**−**D** and of a bulk sample of haematite. In case of haematite the amplitude is multiplied by a factor of 0.3.

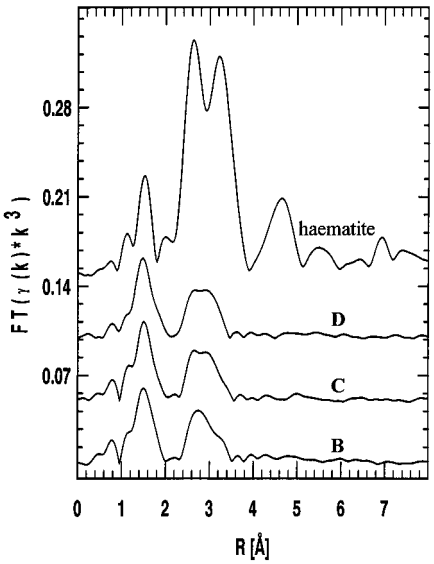

Figure 5. Fourier transforms of the Fe K-edge EXAFS oscillations $\chi(k)*k^3$ of the host/guest compounds **B**−**D** and of a bulk sample of haematite.

shells up to 3.6 Å, which are divided into subshells due to the distortion of the FeO_6 octahedra and the different ways they are linked together.[51] While the Fe−O shells are almost unchanged, the Fe−Fe shells (>2 Å) are slightly shrunk and strongly reduced in intensity caused by the reasons just mentioned above. For further investigations, we have concentrated our work on the Fe−Fe shells to obtain information on the range of structural order within the iron oxide nanoparticles.

Bulk haematite, which is isostructural with corundum, can be described as consisting of hcp arrays of oxygen ions with two-thirds of the octahedral sites filled with Fe(III) ions.[52] The arrangement of cations produces pairs of FeO_6 octahedra. Each octahedron shares edges with three neighboring octahedra in the same plane and one face with an octahedron in an adjacent plane. In addition to the face-shared, different corner-shared octahedra exist between the layers. Depending on the

Table 2. Refined Structure Parameters of the Fe−Fe Coordination Shells, Extracted from the Fe K-EXAFS of Fe_2O_3/MCM-48 Host/Guest Compounds, and Bulk Haematite[a]

sample	N	R (Å)	$\Delta\sigma^2$ (Å^2)	N	R (Å)	$\Delta\sigma^2$ (Å^2)
B ($\Delta E_0 = 3.5$)	0.91	3.00	0.004	0.87	3.12	0.0036
C ($\Delta E_0 = 3.9$)	0.98	2.99	0.003	1.12	3.13	0.003
D ($\Delta E_0 = 3.2$)	1.11	2.99	0.004	1.19	3.12	0.004
haematite ($\Delta E_0 = -1.6$)	0.91	2.91	0.0025	2.95	2.97	0.0039
haematite (s.c.)[53]	1	2.90	-	3	2.97	-
B	0.45	3.48	0.0034			
C	0.51	3.46	0.004			
D	0.50	3.44	0.0036			
haematite	2.80	3.37	0.0034	3.12	3.70	0.002
haematite (s.c.)[53]	3	3.36	-	6	3.71	-

[a] Abbreviations: N = coordination number; R = bond length; $\Delta\sigma^2$ = Debye−Waller factor; ΔE_0 = energy shift; **B**−**D** corresponds to 1−3 impregnation/calcination cycles; s.c. = single-crystal data.

type of linkage between the octahedra, the Fe−Fe distances differ in the following sequence (face-shared < edge-shared < corner-shared). In case of crystalline haematite[53] four different Fe−Fe coordinations shells exist within the range of 2.9−3.7 Å (see Table 2). While the nearest (2.90 Å) and next-nearest (2.97 Å) neighbor shells are formed by face- and edge-shared octahedra, respectively, the other two (3.36 and 3.71 Å) are due to a corner-shared linkage. For further data analyses the Fe−Fe coordination shells were extracted by Fourier filtering using a Bessel window ranging from $R = 2.3$−3.5 Å. Refined structure parameters were obtained by fitting the obtained backtransforms (BTs) in k-space within the range of $k = 3.0$−14.8 Å^{-1} using three shells representing three different Fe−Fe linkages. In case of bulk haematite, four shells were used. To keep the number of independent parameters as small as possible during the refinements, some conditions with respect to the variables had to be made: (1) the amplitude reduction factor was always kept constant to one; (2) the energy shift ΔE_0 was the same for each shell; and (3) the Debye−Waller factors were constrained within the range of 0.002−0.0045 Å^2.

In general, the number of independent degrees of freedom in a spectrum is given by[54] $N_{ind} = (2\Delta k \Delta R/\pi) + 2$. In all cases, the number of parameters used in the fits was always significant smaller than the calculated value of N_{ind}.

To check the accuracy of the least-squares refinements, we also fitted the data of the bulk haematite, which were treated in the same way as the data of the samples **B**−**D**. The received results are in nice agreement with the values obtained from single-crystal XRD data as listed in Table 2. A comparison of X-ray absorption spectroscopic data of the samples **B**−**D** with goethite (α-FeOOH, not depicted) excludes the major formation of this—strongly related to haematite—corresponding oxide hydroxide.[51,52] The reduced coordination number of the Fe−Fe shell at 3.71 Å is probably caused by a slight structural disorder. Figure 6 shows the described BTs (Fe−Fe coordination shells) of each compound together with the results of the least-squares refinements. As one can see, the differences

(51) Manceau, A.; Drits, V. A. *Clay Miner.* **1993**, *28*, 165.
(52) Cornell, R. M.; Schwertmann, U. *The Iron Oxides*; VCH Verlagsgesellschaft: Weinheim, 1996.
(53) Blake, R. L.; Hessevick, R. E.; Zoltai, T.; Finger, L. W. *Am. Mineral.* **1966**, *51*, 123.
(54) Stern, E. A. *Phys. Rev. B* **1993**, *48*, 9825.

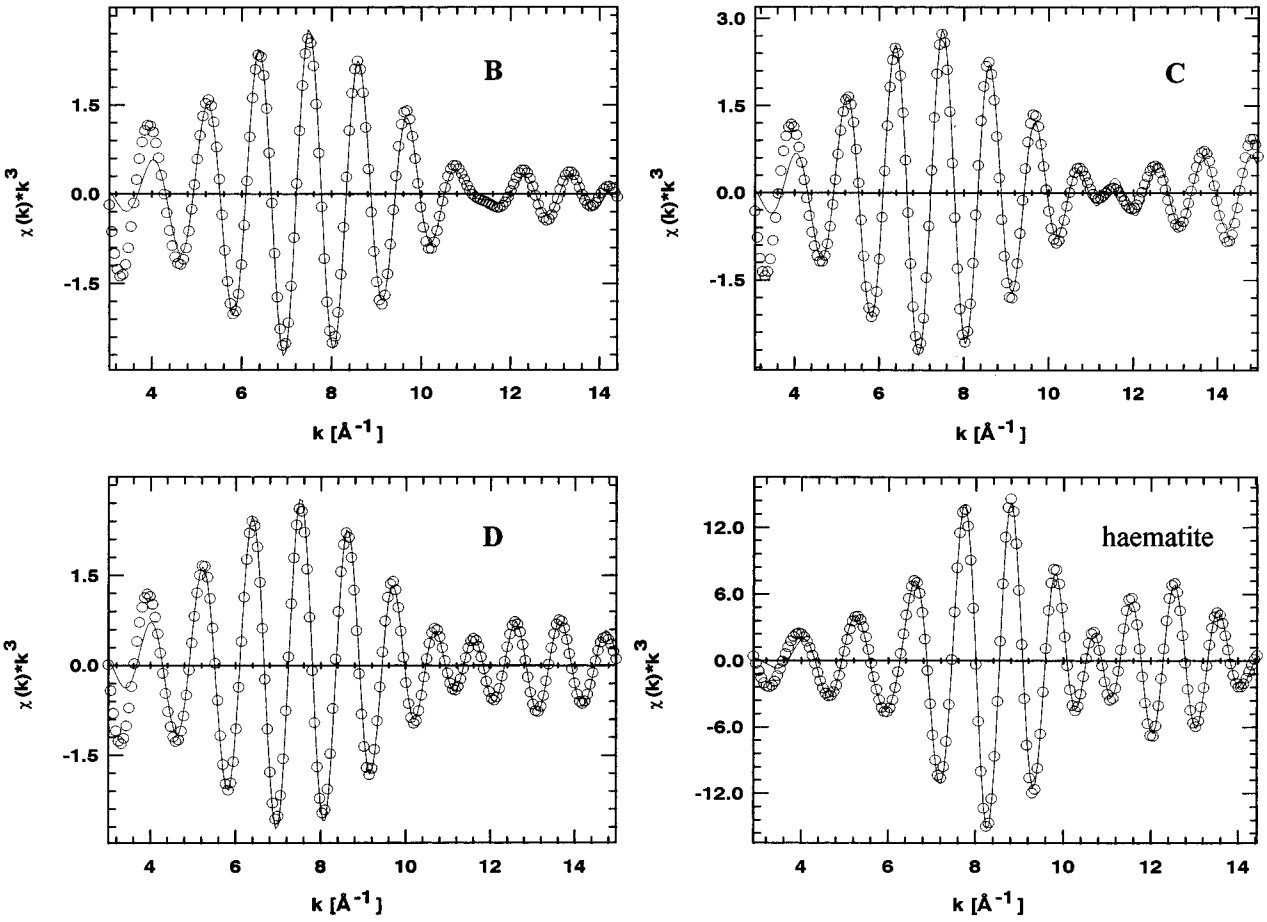

Figure 6. Back-transforms (circles) of the Fe−Fe coordinations shells (ΔR = 2.3−3.5 Å) shown in Figure 5 and the results of the least-squares refinements (solid lines) of the host/guest compounds **B**−**D** and of a bulk sample of haematite.

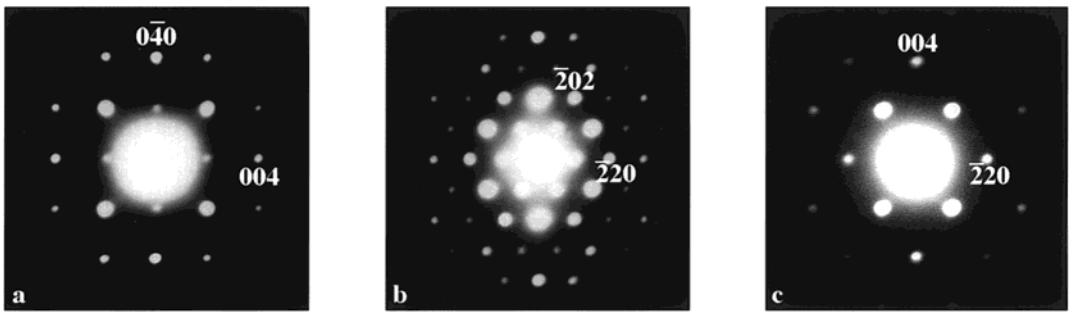

Figure 7. Selected area electron diffraction patterns (SAED) of pristine MCM-48 silica material: (a) ⟨100⟩, (b) ⟨111⟩, and (c) ⟨110⟩ zone axis patterns.

between the experimental and fitted data are marginal. Small deviations at low *k*-values can probably be attributed to the restricted parameter of the energy shift ΔE_0 (see above). This parameter has its strongest influence at low *k*-values.[55] In contrast to the bulk haematite, the first Fe−Fe shell of the nanoparticles appears at 3 Å, a distance which can only be formed by edge-shared octahedra. Even after three impregnation/calcination cycles, the host/guest compound does not contain any face-shared FeO_6 octahedra. In addition, the other two Fe−Fe shells of the nanoparticles occur at distances of ∼3.12 and 3.46 Å, which corresponds to an edge- and corner-shared linkage. With an increasing number of impregnation/calcination cycles, the third Fe−Fe shell becomes shorter, a phenomenon which can probably be attributed to a tempering effect due to the multiple heat treatments. The coordination numbers for each shell are relatively small compared to those in haematite, indicating the small size of the iron oxide nanoparticles within the mesopores of MCM-48.

Electron Microscopy. Two samples, MCM-48 pristine silica material and the (**C**) compound (two impregnation/calcination cycles), were studied by electron diffraction (ED), high-resolution electron microscopy (HRTEM) and qualitative microanalysis (EDS).

Pristine MCM-48 Silica Material. Three electron diffraction patterns of the same crystallite (the ⟨100⟩, ⟨111⟩, and ⟨110⟩ section) are presented in Figure 7. Together with other patterns, they allow reciprocal space to be reconstructed and the determination of the

(55) Teo, B. K. *EXAFS: Basic Principles and Data Analysis*; Springer-Verlag: Berlin, 1986.

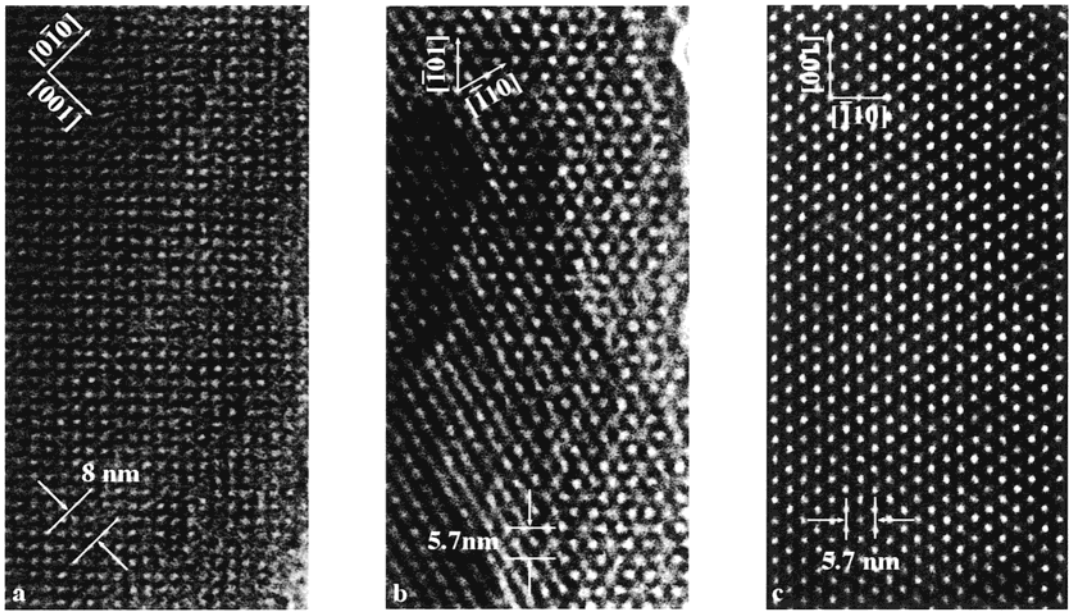

Figure 8. HRTEM images of pristine MCM-48 silica material corresponding to the (a) ⟨100⟩, (b) ⟨111⟩, and (c) ⟨110⟩ zone axes.

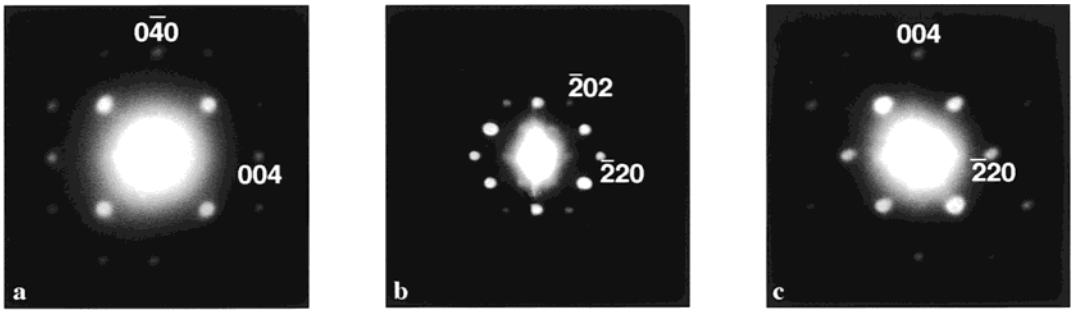

Figure 9. Selected area electron diffraction patterns (SAED) of the host/guest compound **C**: (a) ⟨100⟩, (b) ⟨111⟩, and (c) ⟨110⟩ zone axis patterns.

cubic I-centered Bravais lattice with the following reflection conditions: hkl, $h + k + l = 2n$; hhl, $2h + l = 4n$; and $0kl$, $k = 2n$. These reflection conditions are only compatible with the $I4_1/a\bar{3}2/d$ space group (no. 230), which is in agreement with previous results.[2−4] The {200}and {110} reflections, respectively, present in the ⟨100⟩ (Figure 7a) and the ⟨111⟩ zone axis pattern (Figure 7b), are forbidden reflections which appear due to multiple diffraction; therefore these reflections do not appear on the ⟨110⟩ zone axis pattern (Figure 7c). These electron diffraction patterns, which are taken with a very large camera length, allow the lattice parameter to be estimated as $a = 8.0 \pm 0.1$ nm; a value which is slightly smaller than the one determined from XRD data ($a = 8.5$ nm as seen in Figure 1).

Modern electron microscopy allows resolution even below the 0.2-nm level. Because of the large lattice parameters of MCM-48, high-resolution images can, in principle, be obtained along almost all zone axes. However, the limiting factor for resolution here is no longer the interatomic distance, but the stability of the sample under high voltage illumination. The present images were obtained under low dose conditions with direct magnifications not exceeding 10^5. The most informative images, corresponding to the ⟨100⟩, ⟨111⟩, and ⟨110⟩ zone axes are presented in Figure 8. The images reveal the pore architecture of the material and are characteristic of this kind of material.[3] The crystals are remarkably perfect, and no one- or two-dimensional crystal defect has been detected.

The microanalysis results show the presence of mainly Si, O, and C. The latter element may be intrinsic to the specimen itself, but certainly there is a contribution from the carbon grid and from the contamination which occurs during the recording of the analysis spectrum. In some grains, traces of Cl have been observed.

*Fe_2O_3/MCM-48 Silica Host/Guest Compound (**C**).* Very similar selected area electron diffraction patterns as those observed for the pristine MCM-48 silica material are obtained for the iron oxide-doped material. The zone axis patterns ⟨100⟩, ⟨111⟩, and ⟨110⟩ are presented in Figure 9. The forbidden reflections such as {200} and {110}, which appear due to multiple diffraction, are the same but are less visible than in the previous undoped material. The space group of the structure is still $I4_1/a\bar{3}2/d$, and there is no significant change in the lattice parameter. However, the fact that the diffraction patterns are less pronounced and that higher order reflections are less prominent points to some disorder in the structure. EDS measurements indicate that most of the iron oxide has indeed entered the mesoporous silica phase. However, since no superstructure reflections or any extra diffuse intensity out of the Bragg reflections are observed (see above), we have to assume

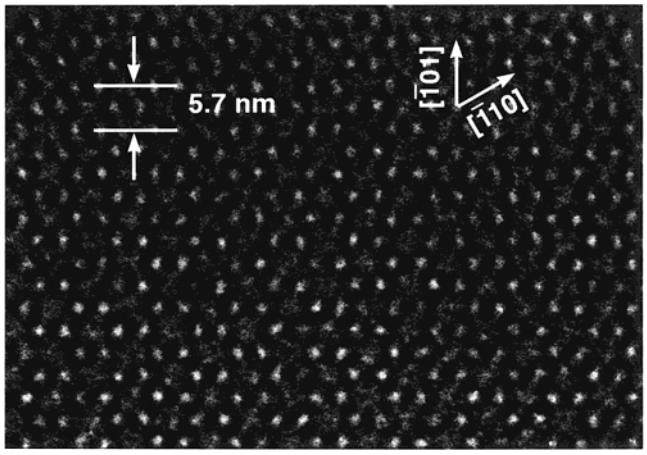

Figure 10. HRTEM image of the host/guest compound **C** corresponding to the ⟨111⟩ zone axis.

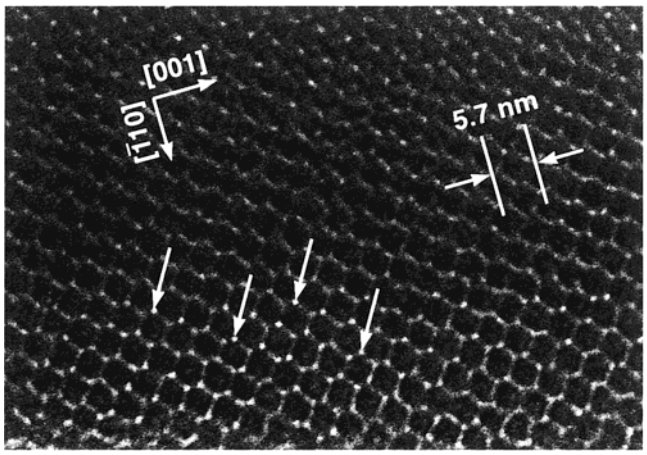

Figure 11. HRTEM image of the host/guest compound **C** corresponding to the ⟨110⟩ zone axis.

that the iron oxide is randomly distributed within the structure.

High-resolution images corresponding to the ⟨111⟩ and ⟨110⟩ zone axis are shown Figures 10 and 11, respectively. At first sight, the high-resolution images look very similar to the ones recorded for the pristine material. However closer inspection reveals intensity deviations and extra bright intensity within the pores (indicated by the arrows in Figure 11). However, not all pores show this contrast, indicating that the Fe_2O_3 filling is not equivalent in all pores. The filling of the pores is also random, without any large structural order, eventual ordering would be readily observed by electron diffraction. This confirms the result obtained from the adsorption/desorption measurements. The intensity deviations and extra intensity within the pores are particularly visible on the images corresponding to the ⟨111⟩ and ⟨110⟩ zone axes; much less along other zone axes. A direct comparison between the ⟨111⟩ image corresponding to the MCM-48 pristine material (Figure 8b) and the one corresponding to the doped material (Figure 10) can be made since the defoci of both images are very similar. The extra intensity modulations have never been observed for the pristine material; together with the detection of Fe and O within the crystallites, this is very strong evidence for the hypothesis that the extra intensity has to be associated with the Fe_2O_3 doping.

The EDS analysis shows, apart from the presence of Si, O, C, Fe, and sometimes traces of Pt. The amount of Fe varies from one grain to the other, indicating that the Fe content is inhomogeneous. We should note that precipitation of Fe−O particles has also been detected, but only as small impurities. After three impregnation/calcination cycles the general aspect remains, only more Fe−O precipitation is observed.

Conclusions

Using the wet impregnation technique iron(III) nitrate was introduced into the mesopores of MCM-48 silica phases. In a sequential combination of drying and calcination procedures, we were able to synthesize haematite nanoparticles more or less exclusively within the pore system. Nitrogen adsorption/desorption measurements still revealed mesoporosity for the host/guest compounds although a reduction of the BET surface area and the pore radius occurs, both being indications of a decoration/coating of the inner surface of the silica walls. X-ray absorption spectroscopic measurements were carried out to obtain information on the local order around the iron atoms. While the analysis of the XANES revealed the occurrence of iron(III) ions, comprehensive EXAFS analyses proved the existence of small slightly disordered iron oxide nanoparticles, in which FeO_6 octahedra are less strongly linked together than in bulk haematite. HRTEM investigations supported the synthesis of a host/guest compound by showing that the mesoporous host structure is still intact after the impregnation/calcination cycles. In addition, no diffuse intensity or superlattice reflections were observed by selected area electron diffraction, indicating that the iron is randomly distributed within the pore structure and not present in a crystalline state. Random intensity deviations and extra intensity modulations within the pores show that the iron oxide filling is not equivalent in all pores. In conclusion, it was shown that the combination of X-ray absorption spectroscopy, HRTEM/SAED, and nitrogen adsorption/desorption measurements is very powerful and that these techniques clearly demonstrate that iron(III) oxide nanoparticles have been formed within MCM-48 silica phases.

Acknowledgment. We thank Professor Armin Reller for continuous support. Financial support by the University of Hamburg, the Swiss Federal Energy Agency, the Werner-Ranz Foundation, the Deutsche Forschungsgemeinschaft (Fr 1372/1-1, Fr 1372/2-1), and the Fonds der Chemischen Industrie is gratefully acknowledged. G.B thanks the European Exchange Program for Students (ERASMUS) for a scholarship. The electron microscopic work has been performed within the framework of IUAP4/10 of the Belgian government. We thank HASYLAB@DESY for allocating beamtime (project number: II-96-85) and Dr. M. Tischer (HASYLAB) for help during the XAS measurements.

CM991048I